



HAL
open science

Accurate unsupervised estimation of aberrations in digital holographic microscopy for improved quantitative reconstruction

Dylan Brault, Thomas Olivier, Ferréol Soulez, Sachin Joshi, Nicolas Faure,
Corinne Fournier

► To cite this version:

Dylan Brault, Thomas Olivier, Ferréol Soulez, Sachin Joshi, Nicolas Faure, et al.. Accurate unsupervised estimation of aberrations in digital holographic microscopy for improved quantitative reconstruction. *Optics Express*, 2022, 30 (21), pp.38383-38404. 10.1364/oe.471638 . hal-03829725

HAL Id: hal-03829725

<https://hal.science/hal-03829725>

Submitted on 25 Oct 2022

HAL is a multi-disciplinary open access archive for the deposit and dissemination of scientific research documents, whether they are published or not. The documents may come from teaching and research institutions in France or abroad, or from public or private research centers.

L'archive ouverte pluridisciplinaire **HAL**, est destinée au dépôt et à la diffusion de documents scientifiques de niveau recherche, publiés ou non, émanant des établissements d'enseignement et de recherche français ou étrangers, des laboratoires publics ou privés.

Accurate unsupervised estimation of aberrations in digital holographic microscopy for improved quantitative reconstruction

DYLAN BRAULT,¹ THOMAS OLIVIER,¹ FERRÉOL SOULEZ,² SACHIN JOSHI,¹ NICOLAS FAURE,³ CORINNE FOURNIER,^{1,*}

¹Univ. Lyon, UJM-Saint-Etienne, CNRS, Institut of Optics Graduate School, Laboratoire Hubert Curien UMR 5516, F-42023, Saint-Etienne, France

²Univ. de Lyon, Université Lyon1, ENS de Lyon, CNRS, Centre de Recherche Astrophysique de Lyon, UMR 5574, F-69230 Saint-Genis-Laval, France

³bioMérieux, Centre Christophe Mérieux, F-38024 Grenoble, France

*corinne.fournier@univ-st-etienne.fr

Abstract: In the context of digital in-line holographic microscopy, we describe an unsupervised methodology to estimate the aberrations of an optical microscopy system from a single hologram. The method is based on Inverse Problems Approach reconstructions of holograms of spherical objects. The forward model is based on a Lorenz-Mie model distorted by optical aberrations described by Zernike polynomials. This methodology is thus able to characterize most varying aberrations in the field of view in order to take them into account to improve the reconstruction of any sample. We show that this approach increases the repeatability and quantitativity of the reconstructions in both simulations and experimental data. We use the Cramér-Rao lower bounds to study the accuracy of the reconstructions. Finally, we demonstrate the efficiency of this aberration calibration with image reconstructions using a phase retrieval algorithm as well as a regularized inverse problems algorithm.

© 2022 Optica Publishing Group under the terms of the [Optica Publishing Group Publishing Agreement](#)

1. Introduction

Optical microscopy can be used to extract several characteristics from a biological sample, such as morphological parameters, birefringence or a phase shifts introduced by an unstained sample. For quantitative measurement of these properties, an accurate optical model is required [1]. Accounting for the characteristics of the optical system is an essential component of reconstruction algorithms in optical microscopy. For example, in fluorescence microscopy, accurate modeling of the Point Spread Function (PSF) is a way to improve the deconvolution step [2–5]. It can be performed using either a dedicated calibration step (by directly measuring the PSF on “point-like” objects [2]) or by estimating the PSF directly on an image that presents aberrations [4,6,7]). In the literature, estimating aberrations or PSF have been widely addressed using various microscopy methods (fluorescence, single-molecule localization, wide-field microscopy, holography, etc.), with different measurement or reconstruction approaches and models of the PSF. These models can be very simple (*e.g.* Gaussian model), more realistic, like the Gibson-Lanni model [5,7,8], or more versatile and general, like the Zernike polynomials of the pupil function [6,9,10]. In the two latter cases, the coherent PSF is modeled as a phase error function in the exit pupil plane of the objective.

In the particular case of digital holographic microscopy, the issues of aberrations estimation and correction have been widely studied for off-axis configuration (*e.g.* [11–14]). However, it concerns essentially the wavefront mismatch between the object and the reference beams, which creates distortions of the interference fringes, thus inducing errors in the reconstruction.

In-line digital holographic microscopy requires a simpler setup involving a single beam. It

45 simply consists in recording the intensity pattern diffracted by a sample. It is less bulky and
46 less sensitive to vibrations than off-axis holographic setups [15, 16]. Image processing makes
47 it possible to reconstruct the optical properties of the sample including its absorption and its
48 phase shift. These can be discriminant in a classification task and makes possible medical
49 diagnoses [17].

50 The aberrations of an in-line holographic optical system can have different causes, such
51 as non standard uses of the objective, tilts or collimation errors in the illumination. These
52 aberrations are dependent on the setup, its alignment and vary in the field of view. They lead to
53 reconstruction errors, not only in the quantitative estimation of the modulus and the phase but also
54 in the geometrical properties of the reconstructed objects. Thus, the repeatability as well as the
55 reproductibility of the reconstructions is affected. However, the aberrations of the optical system
56 are usually not considered in the reconstruction step. Accounting for the aberrations in the image
57 formation model makes it possible to reduce the bias introduced in the reconstructions. These
58 aberrations are an important issue to overcome in applications such as medical diagnoses that
59 require reconstructions to be as accurate as possible to make the decision as robust as possible. To
60 our knowledge, it is only recently that the influence of optical aberrations has been studied in the
61 context of in-line digital holographic microscopy [1, 18, 19]. These studies underlined the need
62 for a fine estimation of aberrations in order to improve the quantitativity and the repeatability
63 of the phase reconstructions as well as the axial positioning, by reducing the aberration-driven
64 biases.

65 In the present paper, we first address the problem of estimating aberrations in the context of
66 in-line digital holographic microscopy. To that end, we use calibration beads to estimate an
67 aberrated forward model. Using an Inverse Problems Approach (IPA), we simultaneously fit
68 Zernike coefficients and calibration beads parameters, which are parameters of the forward model,
69 on data. Unlike many PSF estimation studies, our approach does not require axial stacks of
70 images *i.e.* only one hologram is needed. Moreover, we made no assumption of an aberration-free
71 PSF in the center of the field, like in Zheng's *et al.* study [10]. Finally, this model of aberration is
72 more general than the Gibson-Lanni model [5, 7, 18]. As a forward model, we use a Lorenz-Mie
73 model of the calibration beads that has been extended to account for the aberrations of the optical
74 system using Zernike polynomials [9]. To jointly estimate the calibration beads and aberration
75 parameters, we choose a parametric IPA as it is known to be accurate in estimating the parameters
76 of simple shape objects [20–22] and of the experimental parameters required for calibration. It
77 has already been successfully applied in the context of autofocusing [23], for the estimation of
78 the spectral crosstalk on a Bayer sensor [24] and to estimate the parameters of an astigmatic
79 reference wave [25].

80 Once Zernike coefficients estimated locally for each bead, they can be used to perform
81 aberration free reconstruction of the sample. These reconstructions can be performed using
82 regularized IPA algorithm [26,27] or Fienup algorithm [28,29]. To test the proposed methodology,
83 we use the experimental procedure of Martin *et al.* in [18], *i.e.* the use of a water immersion
84 microscope objective with a correction collar that causes aberrations when not set correctly.

85 In the following section, we describe the method to estimate aberration parameters (Zernike
86 coefficients) and use them to refine the PSF model of our holographic setup in order to reconstruct
87 aberration-free images. In the third section, we detail the setup used to validate the proposed
88 methodology. In the fourth section, to demonstrate the robustness of the approach to reconstruct
89 various kinds of aberrations, we first present the estimation of both aberrations and beads
90 parameters on simulated holograms and on experimental holograms. Finally, to illustrate the
91 relevance of our approach on experimental data, the experimental data are reconstructed with
92 phase retrieval algorithms (Fienup and regularized IPA algorithms) that take into account the
93 estimated aberrations.

94 2. Estimation of the aberration parameters and reconstruction

95 Inverse problems are a general class of problems where unknowns are linked to measurements
 96 through a known image formation model (simulating the measurements is referred to as the
 97 “forward problem”). In this framework, reconstructions are based on minimizing the discrepancy
 98 between the hologram (the data) \mathbf{d} and an image formation model (forward model) \mathbf{m} . In a general
 99 case, such phase retrieval problem is ill-posed as it has many degeneracies (more unknowns than
 100 data, twin image, *etc.*). To solve it, it is necessary to inject some *a priori* on the solution into the
 101 minimization problem by adding regularization terms and/or constraints. Another way to solve
 102 this degeneracies is to use a model of the measurement that depends on only a few parameters.
 103 The problem can be then solved using the parametric IPA framework [30]. This framework
 104 is well suited to calibrate the aberrations using holograms of spherical objects as the image
 105 formation model depends only on the parameters of the objects (position, diameter and refractive
 106 index) and on the aberrations that can be modeled with a complex pupil function described
 107 by few parameters. Once these aberrations are estimated, they can be used in a regularized
 108 reconstruction method to reconstruct any sample without any aberration artefacts. Figure 1
 109 shows a flowchart representing the two main steps, the calibration and the reconstruction, that are
 110 detailed here after.

111 2.1. Calibration : aberration parameters estimation

112 The diffraction pattern $\underline{\mathbf{a}}^{\text{Mie}}$ of a spherical bead is accurately modeled by the Lorenz-Mie
 113 model [31] which depends on the set of bead parameters $\boldsymbol{\vartheta} = \{x, y, z, r, n\}$, where x, y, z
 114 corresponds to the 3D position, r is the radius and n is the refractive index. The Lorenz-Mie
 115 model has been successfully used to reconstruct spherical objects from holograms by fitting
 116 methods [20, 22] or, in a more general framework, by parametric IPA [21, 32, 33]. In the presence
 117 of aberrations, the new image formation model of the diffraction pattern of the beads \mathbf{m}^{P} (P
 118 stands for Parametric) also depends on the aberration parameters $\boldsymbol{\alpha}$ of the optical system that can
 119 be included in the model by mean of a complex pupil plane as follows:

$$120 \mathbf{m}^{\text{P}}(\boldsymbol{\vartheta}, \boldsymbol{\alpha}) = \left| \mathcal{F}^{-1} \left[\underline{\tilde{p}}(\boldsymbol{\alpha}) \odot \underline{\tilde{\mathbf{a}}}^{\text{Mie}}(\boldsymbol{\vartheta}) \right] \right|^2 \quad (1)$$

121 where \mathcal{F}^{-1} is the inverse Fourier Transform, $\underline{\tilde{p}}(\boldsymbol{\alpha})$ is the pupil function in Fourier domain
 122 that depends on (κ_x, κ_y) , the spatial frequency coordinates. For the sake of compactness,
 123 Fourier space coordinates and spatial coordinates are omitted in the equations when they are not
 124 required. $\boldsymbol{\alpha} = \{\alpha_n^m\}_{(m,n) \in \mathbb{Z}^2}$ is a vector of aberration parameters, that will be referred as Zernike
 125 coefficients in this work. $\underline{\tilde{\mathbf{a}}}^{\text{Mie}}$ is the Fourier Transform of $\underline{\mathbf{a}}^{\text{Mie}}$, and \odot is the Hadamard product.

126 As described in [9, 34], Zernike polynomials $\{\mathbf{Z}_n^m\}_{m,n}$ provide a suitable basis to describe the
 pupil function $\underline{\tilde{p}}$ (see Appendix A for details):

$$127 \underline{\tilde{p}}(\kappa_x, \kappa_y, \boldsymbol{\alpha}) = e^{i \left[\sum_{n,m} \alpha_n^m \mathbf{Z}_n^m(\kappa_x, \kappa_y) \right]} \quad (2)$$

128 To characterize the aberration effects of the optical system, the Zernike coefficients $\boldsymbol{\alpha}$ have
 129 to be estimated. Assuming a white and Gaussian noise, the maximum likelihood estimation of
 130 model parameters $\{\boldsymbol{\vartheta}, \boldsymbol{\alpha}\}$ of the bead and the aberrations corresponds to a least squares fitting
 problem [20, 32]:

$$131 \left\{ \boldsymbol{\vartheta}^\dagger, \boldsymbol{\alpha}^\dagger \right\} = \underset{\boldsymbol{\vartheta} \in \mathbb{P}, \boldsymbol{\alpha} \in \mathbb{D}}{\text{argmin}} \|\mathbf{d} - \mathbf{m}^{\text{P}}(\boldsymbol{\vartheta}, \boldsymbol{\alpha})\|_2^2 \quad (3)$$

132 where $\{\mathbb{P}, \mathbb{D}\}$ are optimization constraints and $\|\cdot\|_2$ is the L_2 -norm. Note, taking the weighted
 133 version of the L_2 -norm (*i.e.* the squared Mahalanobis distance) makes it possible to consider
 non-stationary and correlated noise into account [32, 35, 36].

To numerically solve this optimization problem (equation 3), only the first 15 Zernike coefficients are estimated in the following. As a phase piston has no effect on the image formation model (intensity image formation model), α_0^0 is set to 0. As varying Zernike coefficients α_1^{-1} and α_1^1 simply amounts to shift parameters x and y , these Zernike coefficients are also set to 0. In these conditions, seventeen parameters are studied:

$$x, y, z, r, n, \alpha_2^{-2}, \alpha_2^0, \alpha_2^2, \alpha_3^{-3}, \alpha_3^{-1}, \alpha_3^1, \alpha_3^3, \alpha_4^{-4}, \alpha_4^{-2}, \alpha_4^0, \alpha_4^2, \alpha_4^4.$$

134 A study of the correlations between the estimated parameters is presented in Appendix B.
 135 It shows some high correlations in the correlation matrix. All the parameters $\{\vartheta, \alpha\}$ should
 136 therefore be estimated simultaneously. An iterative detection/local optimization scheme [21] is
 137 used to guarantee the rapid and accurate reconstruction of a set of objects. Since the beads are
 138 monodispersed, a narrow parameter research domain \mathbb{P} can be chosen depending on the size and
 139 refractive index of the beads used experimentally.

140 Since the aberration can differ depending on the location of the beads in the field of view, the
 141 aberration parameters have to be estimated for several different bead locations.

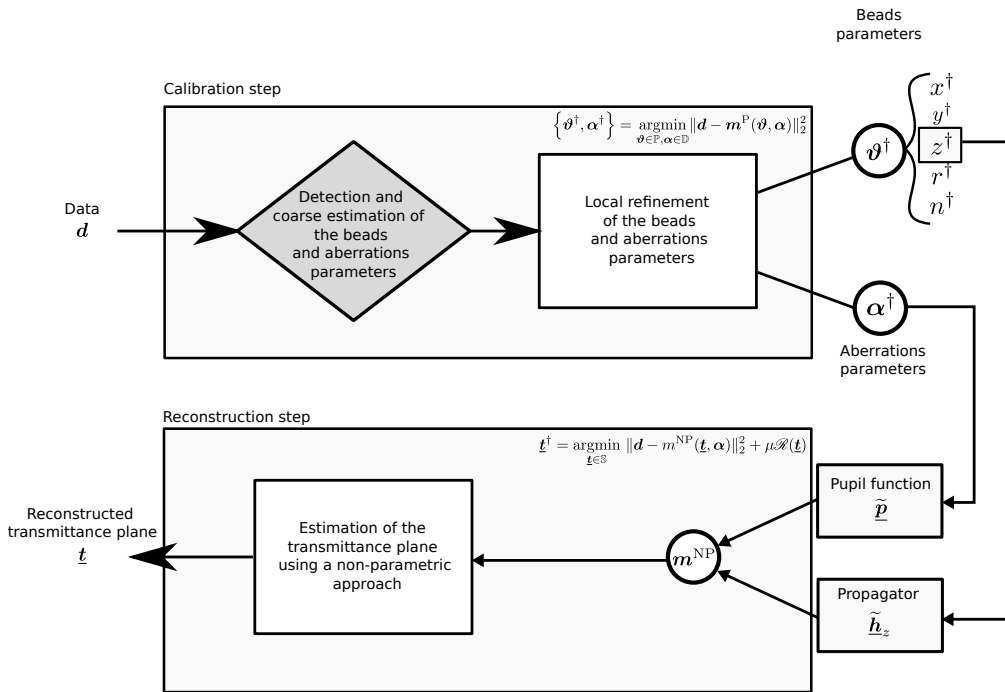


Fig. 1. Flowchart representing the two main steps of the proposed method: calibration and reconstruction.

142 2.2. Reconstruction: including aberration model

143 Once the aberrations are modeled, they are taken into account to better reconstruct the modulus
 144 and the phase of the objects of interest. These samples are modeled by a 2D transmittance plane
 145 $\underline{t}(x, y)$. In that case, the image model will be referred as non-parametric. For an infinite aperture
 146 and aberration free imaging system, this model is the squared modulus of the convolution between

147 the Rayleigh-Sommerfeld propagation kernel $\underline{h}_z^{\text{RS}}$ and the transmittance plane \underline{t} where:

$$\underline{h}_z^{\text{RS}}(x, y) = \frac{z}{i\lambda} \frac{\exp\left(i\frac{2\pi}{\lambda}\sqrt{x^2 + y^2 + z^2}\right)}{x^2 + y^2 + z^2} \quad (4)$$

148 and λ is the wavelength of the illumination [37]. In order to account for aberrations in the
 149 image formation model, an aberrated PSF model should be used. Assuming a shift invariance of
 150 the pupil function with z , the Optical Transfer Function (OTF), which is equal to the Fourier
 151 Transform of the complex-valued PSF \underline{h}_z , can be expressed as follows:

$$\widetilde{\underline{h}}_z(\alpha) = \widetilde{p}(\alpha) \odot \widetilde{\underline{h}}_z^{\text{RS}} \quad (5)$$

152 where $\widetilde{\underline{h}}_z^{\text{RS}}$ is also called the angular spectrum.

153 In addition, the beads estimated depth provides reliable estimation of the propagation distance z^\dagger
 154 [23]. Thus, the aberration corrected non-parametric model \mathbf{m}^{NP} can be expressed as:

$$\mathbf{m}^{\text{NP}}(\underline{t}, \alpha) = |\underline{h}_z(\alpha) * \underline{t}|^2 \quad (6)$$

155 Unlike the parametric case (section 2.1), minimizing the discrepancy between data and model
 156 is not sufficient to solve this ill-posed problem. *A priori* information about the sample must be
 157 added in the form of constraints on the optimization space \mathbb{S} and in the form of a regularization
 158 term \mathcal{R}^{NP} [27, 38, 39]:

$$\underline{t}^\dagger = \underset{\underline{t} \in \mathbb{S}}{\operatorname{argmin}} \|\mathbf{d} - \mathbf{m}^{\text{NP}}(\underline{t}, \alpha)\|_2^2 + \mu \mathcal{R}^{\text{NP}}(\underline{t}) \quad (7)$$

159 where μ is an hyperparameter.

160 This reconstruction is called a regularized reconstruction. The knowledge of the propagation
 161 distance z is crucial because the image formation model depends on it. This distance is
 162 chosen according to the parameters of the beads previously estimated with the parametric IPA
 163 reconstructions [23].

164 In the following, the regularization term is a hyperbolic total variation term [40]. The
 165 hyperparameter is chosen empirically. The optimization domain is restricted to the unitary disk
 166 corresponding to a non-emissive object hypothesis. A FISTA algorithm is used to perform this
 167 minimization [41].

168 3. Experimental study

169 3.1. Principle

170 High quality microscope objectives are supposed to be diffraction limited as long as they are used
 171 in the standard conditions for which they have been optimized (coverslip thickness, refractive
 172 indices of the immersion medium, the sample medium and the coverslip and position of the
 173 sample relative to the coverslip) [8, 42]. Yet, in some applications, these golden rules may be
 174 broken (wrong coverslip thickness, for instance). In inset A of Fig. 2, the refraction of the beam
 175 in the coverslip is shown before entering the objective. This illustrates the origin of the possible
 176 wavefront errors that may occur between the paraxial rays and the high angle rays when the
 177 standard conditions of use are not met. This wavefront error has been described by several
 178 authors [8, 42] in on-axis situations, but it may vary with the position in the field of view. Finally,
 179 even when the rules are strictly applied, residual aberrations may still exist, especially out of the
 180 optical axis, and may differ from one objective to another. To experimentally study the influence
 181 of such aberrations, we used a water immersion objective with a coverslip correction collar. Thus,
 182 for a given coverslip thickness, a wrong correction collar setting will give rise to aberrations.
 183 This idea was recently proposed by Martin *et al.* [18].

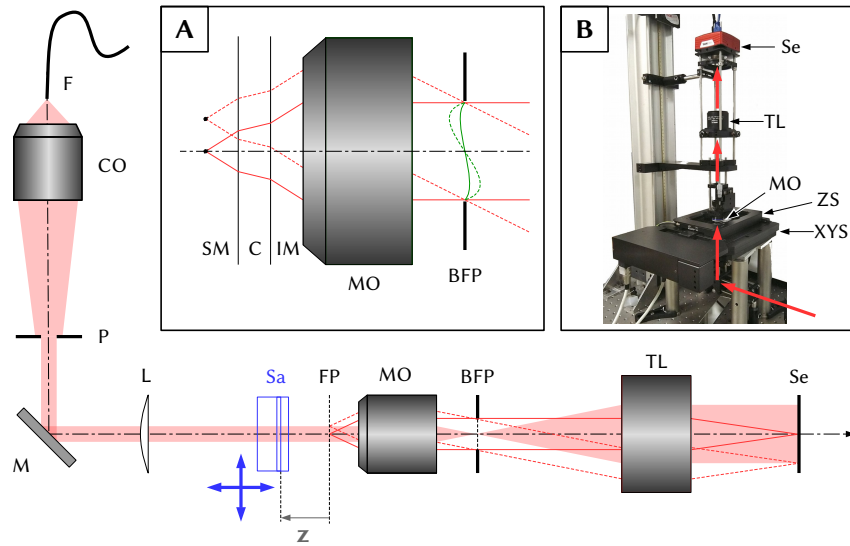


Fig. 2. Experimental setup. F: monomode fiber coupled laser source, CO: collection optics, P: $200\mu\text{m}$ -pinhole, M: mirror, L: lens, Sa: sample that can be precisely moved in XYZ-directions, z: defocus distance of the sample from the focus plane, FP: objective focal plane, MO: microscope objective, BFP: objective back focal plane, TL: tube lens, Se: sensor. **Inset A:** zoom on the sample and the objective showing the refraction of the rays occurring through the coverslip. SM: sample medium, C: coverslip, IM: immersion medium. **Inset B:** Picture of the setup showing the imaging system and the precision piezo-stage (ZS) and the XY-translation stage (XYs).

184 3.2. Setup

185 Our home-made experimental setup [19] is presented in Fig. 2. The setting of a spatially coherent
 186 illumination may be difficult in a microscopy setup as it is very sensitive to any stray reflections
 187 or dust particles and leads to complex, sometime unstable speckle patterns. In this setup, the
 188 coherent illumination is set by illuminating a $200\mu\text{m}$ -pinhole (P) and a lens (L) set in a $2f$
 189 configuration. Thus, an airy pattern illuminates the sample, with a large enough central peak
 190 to illuminate the whole field of view, but without inserting too much stray light in the imaging
 191 system. This leads to moderate vignetting which is corrected by dividing the holograms by a
 192 background intensity image.

193 In the present study, the sample was composed of 1μ -diameter polystyrene beads diluted in
 194 glycerol. The use of transparent beads is interesting here, because we aim at reconstructing
 195 phase objects. The diameter of the beads is chosen to mimic biological objects such as bacteria.
 196 Usually, sub-resolution objects are used for PSF calibrations. However, in our context, with
 197 sub-resolution beads, the contrast of holograms would be too low and Rayleigh-Sommerfeld
 198 based models would fail to reconstruct correctly the beads [43].

199 As polystyrene beads float in glycerol and thanks to its high viscosity, the beads were located
 200 just below the coverslip and did not move during the exposure of one hologram (typically, few
 201 milliseconds). According to the Gibson-Lanni model of the aberrations [8] induced by wrong
 202 coverslip thicknesses and/or refractive indices, the fact that the sample medium was glycerol
 203 instead of water should not induce additional aberrations as the beads were just below the
 204 coverslip (*i.e.* $t_s = 0$ with the Gibson-Lanni notations). A coherent illumination with a laser at

205 637.6nm was used. The illumination power was sufficient to keep exposure times as short as 5ms
 206 with our Thorlabs-S805MU1 camera. The sensor pixel size was $5.5\mu\text{m}$. With 22.6mm diagonal,
 207 the sensor covers an important part of the field of view of the image (the objective field number
 208 is 26.5mm). The microscope objective was a water immersion microscope objective (Olympus
 209 PlanSApo, 60 \times , 1.2NA) with a coverslip correction collar. The tube lens was a 200mm-focal
 210 length apochromatic TTL200MP from Thorlabs that was used in a telecentric configuration. The
 211 measured magnification was 66.5, and not 60, as the tube lens has a greater focal length than the
 212 Olympus standard (180mm).

213 3.3. Experimental protocol

214 Five cases of aberration were tested in this experiment with the correction collar at different
 215 settings (0.13, 0.15, 0.17, 0.19 and 0.21mm). The coverslip thickness was measured to be
 216 0.170mm with a digital indicator (with a resolution of $\pm 1\mu\text{m}$). Thus, the 0.17mm setting of
 217 the correction collar is assumed to be the aberration free situation. A single bead was tracked
 218 through the whole field of view in regular steps in the X and Y directions. A total of 35 images
 219 (7×5) were acquired in order to regularly cover the whole field of view ($273 \times 204\mu\text{m}$). For each
 220 XY-position in the field, an axial stack was recorded with defocus positions ranging from $-10\mu\text{m}$
 221 to $+20\mu\text{m}$ from the focus position with a step size of $0.5\mu\text{m}$. This stack is used for the illustration
 222 of Fig. 3, but only one axial position will be reconstructed in the next section. It should be noted
 223 that the sample is the only moving part, which is important for recording a background image by
 224 calculating the median value of the 35 XY-shifted images recorded at focus.

225 A view of a typical hologram is shown in the top part of Fig. 3. XZ-views of the stack along
 226 the vertical axis of the bead are represented at the bottom of Fig. 3. As shown in the figure, a
 227 change in the focus position is observed as a function of the setting of the correction collar, as
 228 well as modifications in the XY-profiles. The radial symmetry of the PSF is not always valid, as
 229 can be seen, for example, for the 0.13mm setting of the correction collar (green). This asymmetry
 230 is due to aberration effects that may break the radial symmetry of the holograms (*e.g.* coma,
 231 astigmatism, etc.). All aberrations may originate from the objective, but also from the tube lens
 232 or from misalignment of the illumination or the imaging parts. Moreover, aberrations can also
 233 originate from inhomogeneities of the slide and the coverslip.

Wavelength	637.6nm
Magnification	66.5
Pixel pitch	83nm
Total field of view	$273 \times 204\mu\text{m}$
Beads diameter*	$(1.0 \pm 0.06)\mu\text{m}$
Beads refractive index*	1.587 (polystyrene)
Refractive index of immersion medium	1.47 (glycerol)
Coverslip thickness	$(0.170 \pm 0.001)\text{mm}$
Typical defocus	$12\mu\text{m}$

Table 1. Experimental parameters (*from manufacturer, ThermoFisher Scientific, Inc.)

234 4. Results

235 In this section, we first apply the proposed method to simulated holograms to demonstrate
 236 the robustness of our approach for several kind of aberrations, especially in cases of difficult

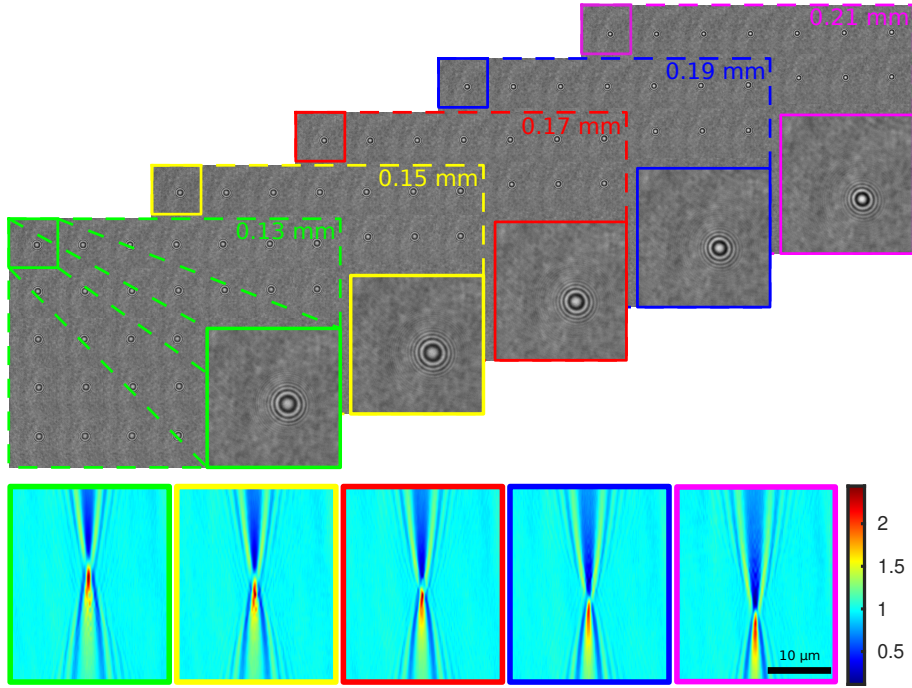


Fig. 3. Example of a mosaic of holograms (top) of $1\mu\text{m}$ -diameter polystyrene beads in glycerol for an approximate defocus of $12\mu\text{m}$ under 5 different settings of the correction collar (from left to right: 0.13 (green), 0.15 (yellow), 0.17 (red), 0.19 (blue) and 0.21mm (magenta)). XZ-views of the hologram stacks for the different correction collar settings (bottom).

237 optimizations, *i.e.* with highly correlated Zernike coefficients. We then apply it to experimental
 238 holograms of beads. We compare our results with state-of-the-art parametric reconstruction
 239 algorithms in both simulated and experimental cases and finally evaluate and discuss the effects
 240 of aberration on regularized reconstructions.

241 4.1. Reconstructions on simulated data

242 A mosaic of 7×5 in-line holograms was simulated with aberrations varying in the field of view
 243 (see Fig. 4). Each hologram is a 512×512 pixels sub-image simulated with the experimental
 244 parameters described in Table 1 and with the aberrated Lorenz-Mie model (see equation 1). The
 245 defocus is set to $12\mu\text{m}$. This distance was chosen to improve the accuracy of the estimation of the
 246 Zernike coefficients, as indicated by CRLB analysis of this parameter (see Appendix B Fig. 11).

247 To simulate a varying PSF in the field of view, the aberrated pupil function was considered
 248 to depend on the position of the bead in the field of view. This pupil function corresponds to a
 249 linear combination of oblique astigmatism (Z_2^{-2}), vertical coma (Z_3^{-1}), horizontal coma (Z_3^1),
 250 spherical aberration (Z_4^0) and oblique secondary astigmatism (Z_4^{-2}) (see Appendix A). This
 251 linear combination is weighted by the corresponding Zernike coefficients α (see Section 2.1).
 252 We arbitrarily chose to set a linear behavior along y for α_2^{-2} and α_3^1 , a linear behavior along x for
 253 α_3^{-1} and α_4^{-2} , and we set α_4^0 constant in the field of view. This set of coefficients was chosen to
 254 demonstrate the performance of the proposed method in difficult cases, *i.e.* we chose Zernike
 255 coefficients that were highly correlated in the corrected model (see Appendix B, Table 6).

256 Finally, a white Gaussian noise ϵ was added to the simulated holograms, which led to a

257 Signal-to-Noise Ratio (SNR) of 4 in the holograms ($\text{SNR} = \frac{\Delta m}{2\sigma_\epsilon}$, where Δm is the peak-to-peak
 258 amplitude of the model).

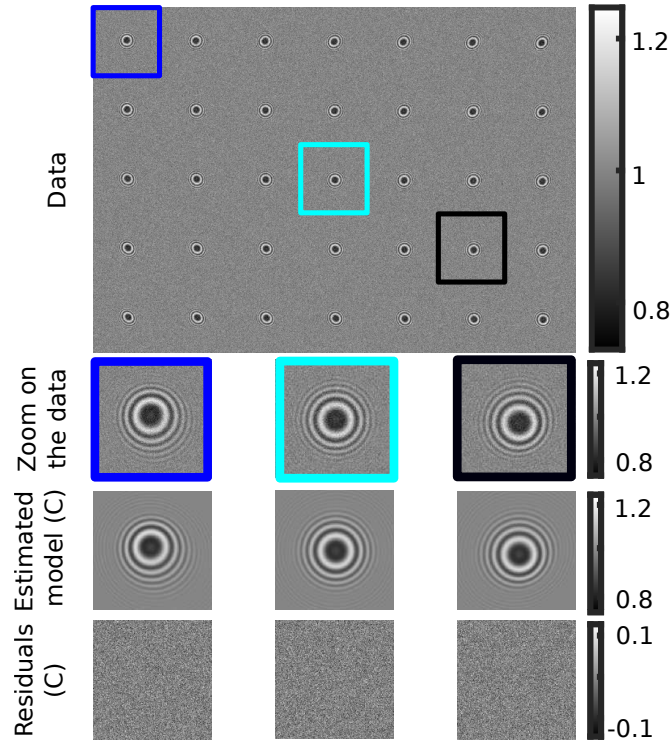


Fig. 4. **Top:** 35 holograms simulated with variable Zernike coefficients depending on the position in the field of view. **Bottom:** magnifications of 3 holograms from different areas (first line), estimated model accounting for aberrations (C)(second line), residuals i.e. difference between the first line and the second one (third line).

259 For each simulated hologram, the reconstruction was performed using parametric IPA with
 260 or without aberration corrections in the model. The abbreviations C (standing for corrected),
 261 and UC (standing for uncorrected) will be used in the following. The optimization algorithm we
 262 used was the LINCOA algorithm [44]. To perform the reconstructions with the corrected model
 263 (C), the first step implies an exhaustive search in a 17 parameters space, which can be really
 264 demanding in terms of computational time. To reduce this exhaustive search, it can be fairly
 265 convenient to have at least a coarse knowledge of the Zernike coefficients. As our aberrations
 266 were quite low, we performed this step by considering no aberration, *i.e.* all Zernike coefficients
 267 were set to zero.

268 Then, the optimization step was performed with the fully corrected model (eq.3), with the
 269 constraints on parameters described in Table 2. The optimization domains $\{\mathbb{P}, \mathbb{D}\}$ were chosen
 270 quite large in order to check the robustness of the proposed method.

271 Table 3 shows the bead parameters reconstructed without (UC) or with (C) taking the aberration
 272 into account in the model. It shows the biases introduced by geometrical aberrations. When
 273 using an unaberrated model (UC), the reconstructions converge either on a local optimization
 274 minimum or to the constraint domain bounds. Conversely, when using an aberrated model, the
 275 reconstructions always converge to the global minimum with low bias and a standard deviation
 276 close to the theoretical lower bound given by Cramér-Rao analysis.

	z	r	n	α_2^{-2}	α_2^0	α_2^2	α_3^{-3}	α_3^{-1}
Lower bound	10	0.2	1.52	-10	-10	-10	-10	-10
Upper bound	14	0.7	1.63	10	10	10	10	10
	α_3^1	α_3^3	α_4^{-4}	α_4^{-2}	α_4^0	α_4^2	α_4^4	
Lower bound	-10	-10	-10	-10	-10	-10	-10	
Upper bound	10	10	10	10	10	10	10	

Table 2. Optimization constraints for each estimated parameters (z and r are in micrometers)

ϑ_i	ϑ_i^{GT}	$\langle \hat{\vartheta}_i \rangle^{UC}$	$\langle \hat{\vartheta}_i \rangle^C$	$\sigma_{\vartheta_i}^{CRLB}$	$\sigma_{\hat{\vartheta}_i}^{UC}$	$\sigma_{\hat{\vartheta}_i}^C$
$z(\mu m)$	12	11.048	12.001	0.002	0.579	0.004
$r(\mu m)$	0.5	0.267	0.500	0.001	0.030	0.001
n	1.58	1.619	1.5798	0.0006	0.0311	0.0007

Table 3. Statistical results on the estimated bead parameters with aberration corrected (C) and uncorrected (UC) models: Ground Truth (GT) parameters ϑ_i^{GT} , means of the estimated parameters $\langle \hat{\vartheta}_i \rangle$, lower bounds of their theoretical standard deviations $\sigma_{\vartheta_i}^{CRLB}$ and standard deviations of their estimates $\sigma_{\hat{\vartheta}_i}$

277 Residuals between the data and the model are very low, indicating that the model fits the data
278 accurately (see the bottom line in Figure 4). On the upper part of Fig. 5 are presented the phase
279 of the pupil functions that were simulated in each part of the field of view. This gives another
280 view, in Fourier space, of the type of phase errors that aberrations may imply. On the lower part
281 of Fig. 5 the residuals of the estimated pupil functions are presented (from the simulated ground
282 truth). From these residuals, we see that our estimations of the Zernike coefficients are accurately
283 describing the phase function introduced by aberrations in Fourier space.

284 In the most difficult cases (upper part and lower part of the field on Fig. 5), the residuals are
285 not negligible for the highest spatial frequencies, close to the cutoff frequency imposed by the
286 numerical aperture of the objective (represented by a black dashed circle). Indeed, as we did
287 not use a sub-resolution object, the power spectrum of the object is not filling the entire pupil.
288 In the inset of Fig. 5, the typical power spectrum of the object is presented and a white dashed
289 circle shows the part of the spectrum including 95% of its energy. In this white dashed circle,
290 the residuals remain low. Actually, this is an unsurprising limitation of this approach: as the
291 object spectrum does not cover the whole aperture of the objective, the pupil phase function can
292 not be estimated precisely for the highest frequencies. However, the pupil function is correctly
293 estimated for the spatial frequencies corresponding to the spectrum of the object, which ensures
294 that a similar object will be correctly reconstructed. If the aberrations are important, this effect
295 must be considered for the choice of the calibration objects: the size of the beads chosen for
296 aberration estimation must be at least equal or smaller than the smallest detail of interest.

297 4.2. Reconstructions on experimental data

298 The experimental parameters are given in table 1 and were the same as those used in the simulations.
299 Once again, since the accuracy of the estimated parameters is better in a specific range of defocus z

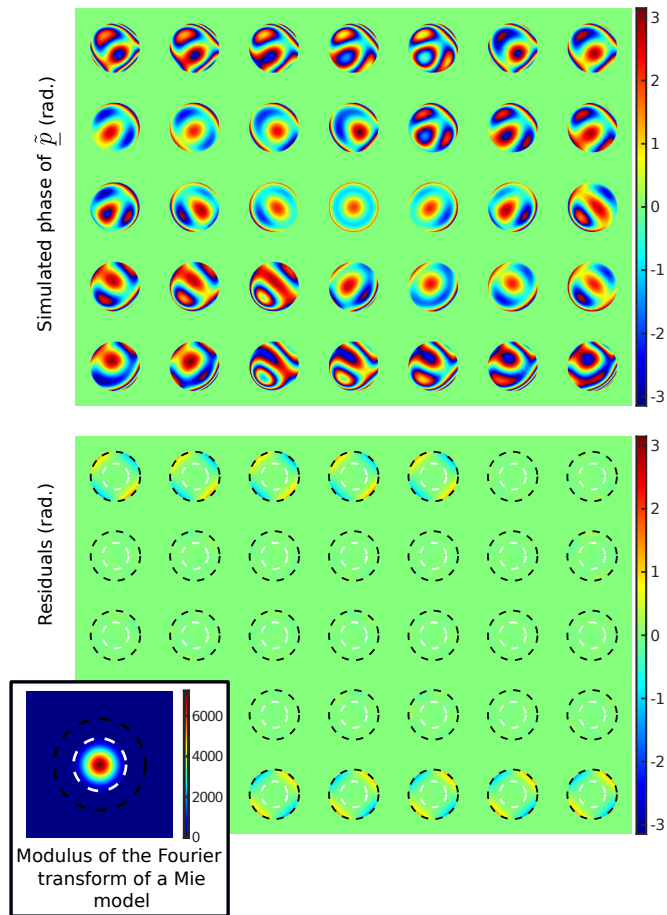


Fig. 5. Simulated phase correction in the pupil planes $\tilde{p}(\alpha^\dagger)$ (a) and residuals of the estimated pupil functions from the ground truth (b). The white dashed circles correspond to the disk in which 95% of the energy of the power spectrum of the object (c) is contained. The black dashed circles correspond to the aperture (calculated from the numerical aperture of the objective).

300 (see Appendix B), the holograms to be reconstructed were located approximately $12\mu\text{m}$ from the
301 focus position, as in the simulations. They were reconstructed using parametric IPA, with the
302 same workflow that was described in the reconstructions of the previous subsection. Again, to
303 compare the effect of aberrations on the estimation of the beads parameters, both corrected (C)
304 and uncorrected (UC) models are used for the reconstructions. As illustrated in Section 3, the
305 position of the focus varied with the setting of the correction collar. Parametric IPA provides an
306 estimation of the defocus distance z between the sample and the focal plane of the objective.

307 Table 4 presents a list of the mean values and the standard deviations of all 35 positions in
308 the field for parameters z , r and n and for both (UC) and (C) reconstructions. According to the
309 comparison of standard deviations for each collar setting, the dispersion over the field was only
310 moderately modified by the model (UC) or (C). However, the mean values changed, especially
311 that of the estimated defocus \hat{z} . A maximum difference of $1.68\mu\text{m}$ in the estimated defocus was
312 found between the two models (UC) and (C).

313 Moreover, the estimated defocus highly depends on the correction collar setting, which varied
314 from 8.8 to $13.9\mu\text{m}$ (UC) and from 10.5 to $12.5\mu\text{m}$ (C). Thus, this dispersion was reduced by
315 taking the aberrations into account, indicating a correction of the bias in the evaluation of the
316 defocus. Since regularized reconstruction algorithms rely on a precise knowledge of the image
317 formation model (including the defocus distance), any misestimation of the axial position of the
318 sample would bias the reconstructions. Finally, it must be noted that the remaining dependence
319 of the estimated defocus with the correction collar setting may have a physical origin. Indeed,
320 wrong settings of the correction collar may really change the focus position as it changes the
321 properties of the objective.

322 For the estimated radii \hat{r} and refractive indices \hat{n} , the dispersion over the field was reduced
323 when the aberrations were taken into account. The averages were also less dispersed, but to a
324 lesser extent. Indeed, some biases that depend on the correction collar setting appeared to remain.

325 Fig. 6 presents the estimated bead parameters as scatter plots. This makes it possible to
326 visualize the correlations between the estimated parameters z , r and n .

327 Moreover, for each collar setting (one color for one collar setting), taking the aberrations into
328 account improved the repeatability of the parameter estimation independently of the introduced
329 aberrations. Indeed, the aberration corrections not only reduce the biases between the different
330 collar settings (differences from one color point cloud to another) but also reduce correlations
331 coefficients between parameter estimations (correlations within one color point cloud). This is
332 presented quantitatively on Table 5, for both models (C) and (UC) and for the less aberrated case
333 (0.17mm). According to Table 5, the decorrelation is particularly important between r and n .

334 According to the manufacturer's specifications, the radius should be $(0.5\pm 0.03)\mu\text{m}$ and the
335 refractive index should be around 1.587 . The estimated parameters obtained with or without
336 an aberration model were within the manufacturer's confidence interval (0.47 - $0.53\mu\text{m}$). It is
337 important to note that the fit with the Mie model is constrained by the spherical hypothesis and
338 thus may be quite robust to errors in the model, contrary to the case of regularized reconstruction
339 that have more degrees of freedom, and will be more sensitive to aberrations, especially to
340 non-radially symmetric ones, as it will be seen later on regularized reconstructions.

341 With the 35 recorded holograms corresponding to 35 bead positions in the field of view, we
342 were able to check that the Zernike coefficients vary in the field of view, following continuous
343 evolutions similar to those described in another work [10]. The Figure 7, illustrates the evolution
344 of the Zernike coefficients associated with oblique astigmatism, defocus, vertical coma, horizontal
345 coma and spherical aberrations. These appeared to be the main components of the aberrated
346 pupil function \tilde{p} . The evolution of these coefficients is continuous and, not surprisingly, increases
347 with increasing errors in the correction collar setting. Vertical coma increases from the left
348 to the right whereas horizontal coma increases from the top to the bottom of the field of view.
349 Spherical aberration and defocus do not depend on the location in the field of view but change

	UC	C	UC	C
Collar	$\langle \hat{z} \rangle$	$\langle \hat{z} \rangle$	σ_z	σ_z
0.13	13.913	12.579	0.802	0.817
0.15	13.049	12.542	0.483	0.440
0.17	11.706	12.046	0.548	0.546
0.19	10.496	11.556	0.510	0.484
0.21	8.838	10.525	0.442	0.495
Collar	$\langle \hat{r} \rangle$	$\langle \hat{r} \rangle$	σ_r	σ_r
0.13	0.526	0.501	0.008	0.005
0.15	0.519	0.505	0.006	0.005
0.17	0.502	0.513	0.007	0.004
0.19	0.495	0.519	0.007	0.003
0.21	0.497	0.522	0.007	0.012
Collar	$\langle \hat{n} \rangle$	$\langle \hat{n} \rangle$	σ_n	σ_n
0.13	1.5733	1.5901	0.0041	0.0029
0.15	1.5773	1.5882	0.0027	0.0024
0.17	1.5856	1.5837	0.0044	0.0022
0.19	1.5902	1.5809	0.0036	0.0023
0.21	1.5878	1.5798	0.0032	0.0046

Table 4. For the 5 correction collar settings, averages $\langle \hat{\vartheta}_i \rangle$ and standard deviations $\sigma_{\hat{\vartheta}_i}$ of the estimated parameter \hat{z} , \hat{r} and \hat{n} using (UC) uncorrected model and (C) aberration corrected model . All lengths are in micrometers.

Uncorrected (UC)				Corrected (C)			
ϑ_i	z	r	n	ϑ_i	z	r	n
z	1	0.02	0.51	z	1	0.03	-0.26
r	0.02	1	-0.56	r	0.03	1	0.01
n	0.51	-0.56	1	n	-0.26	0.01	1

Table 5. Correlation coefficients between the estimated parameters without aberration correction (left) and with aberration correction (right) for a correction collar setting of 0.17mm (less aberrated case)

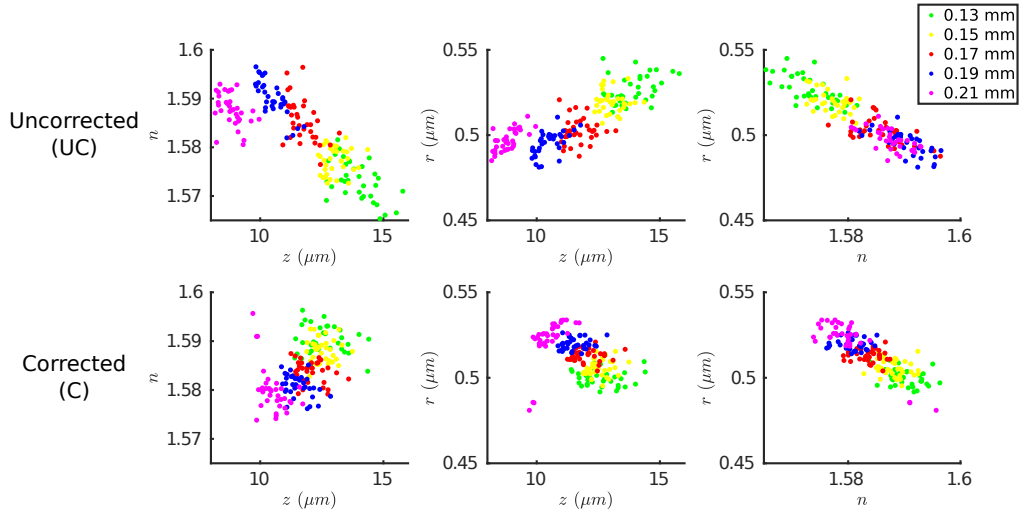


Fig. 6. Scatter plots showing the biases and correlations between the estimated defocus \hat{z} , radius \hat{r} and refractive index \hat{n} for a single bead, for the 35 positions in the field, for the 5 settings of the coverslip correction collar and with corrected models (C) and uncorrected models (UC). With correction of the aberrations, the bias and the dispersion of the estimations due to aberrations are reduced.

350 with the correction collar setting, with almost no spherical aberration and defocus for the less
 351 aberrated case (0.17mm). This is quite logical as a coverslip thickness error is known to induce
 352 spherical aberrations [18]. On the contrary, oblique astigmatism varies in the field of view
 353 without depending too much on the correction collar setting.

354 Figure 8 illustrates the evolution of the phase correction for the 35 positions in the field
 355 of view and for a correction collar of 0.17mm. For this supposedly aberration-free case, the
 356 setup still suffer from aberrations that change in the field of view. These phase functions show
 357 significant aberration effects but, as expected, lower than for the other correction collar settings
 358 (not represented). This indicates the necessity of taking aberrations into account for hologram
 359 reconstruction even when the optical system is supposed to be compensated for aberrations.
 360 Indeed, these aberrations may come from residual aberrations of the objective, but also from
 361 other sources, like thickness inhomogeneities of the slide and the coverslip, as well as alignment
 362 issues.

363 From the numerical point of view, the detection of all 35 beads in the mosaic takes around
 364 30 seconds on a 3296×2472 pixels image. The local optimization step for each bead takes
 365 around 10 seconds when not considering aberrations while it takes 45 seconds when considering
 366 them. These estimations have been realized using an Intel Core i9-11950H CPU 2.60GHz with
 367 16GBytes of RAM.

368 4.3. Reconstructions on experimental data using regularized algorithms

369 The evaluation of aberration's effects on reconstructions is performed using beads holograms.
 370 This allows us to compare quantitatively the reconstructed transmittance with a ground truth
 371 (assumed to be the transmittance of the bead whose parameters are estimated by parametric
 372 IPA). However, since the non-parametric model is very general (not limited to spherical objects),
 373 similar results will be obtained with an aspherical sample. The reconstruction is performed with
 374 (C) and without (UC) the previously estimated aberration pupil function \hat{p} and the \hat{z} parameters.

375 A Fienup phase retrieval algorithm [28, 29], as well as a regularized IPA (as presented in 2.2)

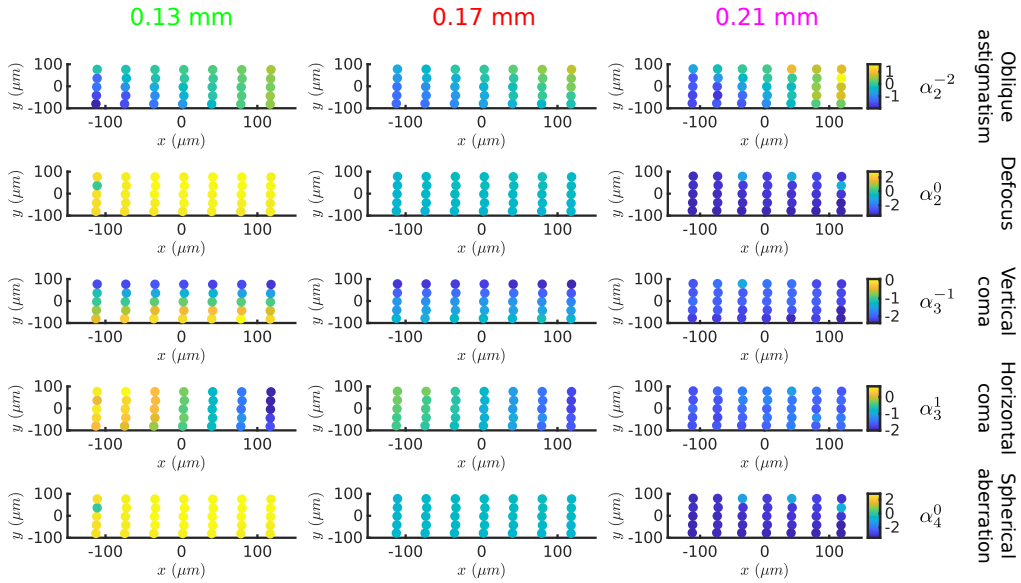


Fig. 7. Estimated Zernike coefficients α_n^m as a function of the position in the field of view and for 3 settings of the coverslip correction collar (0.13 mm, 0.17 mm, 0.21 mm). The evolution of the Zernike coefficients is continuous in the field of view. The coma and astigmatism coefficients depend on the position in the field of view and on the correction collar setting whereas defocus and spherical aberration only depend on the correction collar setting.

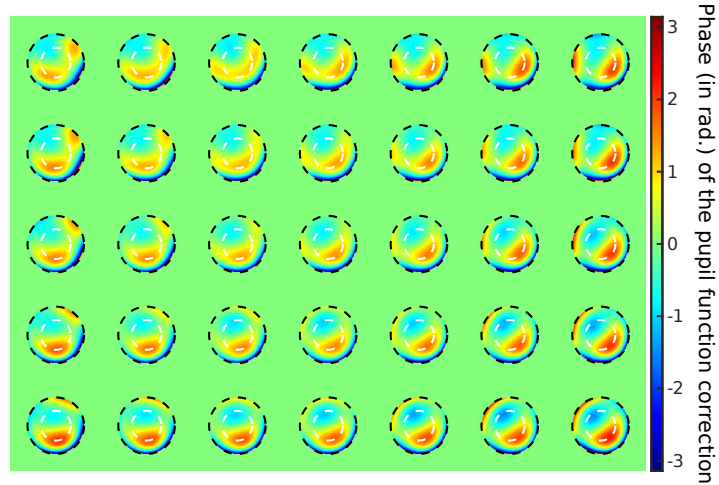


Fig. 8. Evolution of the phase (in radians) of the pupil function correction in the field of view for a setting of the coverslip correction collar of 0.17 mm and for the 7x5 positions in the field where the aberrations were estimated. The black and white dashed circles are defined on Fig.5

376 are used to reconstruct the data. These reconstructions are performed using the uncorrected
 377 propagator $\underline{h}_z^{\text{RS}}$ (UC) or the corrected propagator \underline{h}_z (C) in the model (eq.6). Fig. 9 illustrates
 378 the reconstructions results for both algorithms. The estimated aberrated Mie model that fits the
 379 data has been back propagated at the center plane of the bead (BPMie-C) and is considered as
 380 the ground truth here because it is the most accurate model. Similarly, a back propagation of
 381 the Mie model estimated without aberration has also been computed (BPMie-UC). Because of
 382 the coma aberrations, the bead position (x, y) is not the same for (BPMie-C) and (BPMie-UC)
 383 parametric inversions, as mentioned in Appendix B. For comparison purpose the beads have then
 384 been centered in Fig. 9.

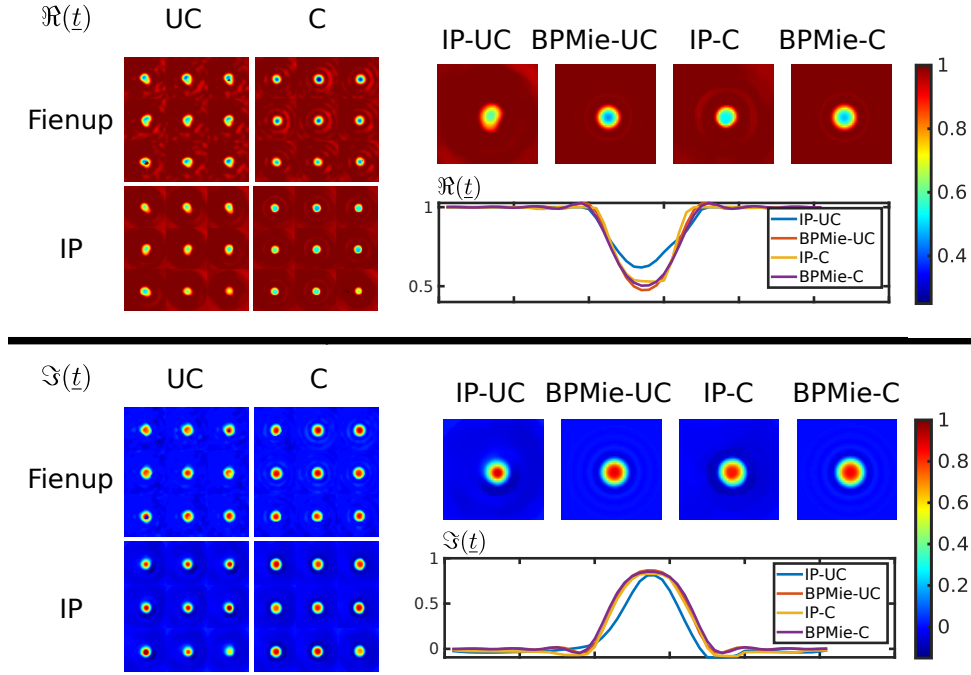


Fig. 9. Non-parametric reconstructions using regularized IPA and Fienup algorithm with (C) or without (UC) aberrations correction. The reconstructions are presented in real part an imaginary part. A reconstruction is compared with the back-propagation of the estimated Mie model without aberration estimation (BPMie-UC) and the back-propagation of the Mie model with aberration estimation (BPMie-C). Profiles of the real part and imaginary part at the center of the bead are presented.

385 When aberrations are not considered in the reconstruction model, the morphological properties
 386 and quantity of the reconstructions are compromised. Indeed, either with Fienup or
 387 regularized IPA, the bead does not show a circular shape. As the aberrations vary in the
 388 field of view, the same bead does not have the same shape for each lateral position. The
 389 back-propagation of the Mie model without aberration illustrates the model error when the
 390 aberrations are not considered, but the radial symmetry is maintained as the Mie model is based
 391 on a spherical model. The regularized reconstructions without aberrations do not match with
 392 this model indicating bias in the estimation of the bead parameters. However, with aberrations
 393 correction the reconstructions fit the corresponding back-propagated Mie model and have the
 394 expected geometrical and quantitative properties. It demonstrates that whatever the reconstruction
 395 algorithm, aberrations should be taken into account to restore accurately the morphological and
 396 quantitative properties of the sample.

397 Taking into account the aberrations in regularized reconstructions has no effect on the
 398 computational time as the aberrated forward model has the same complexity as angular spectrum
 399 propagation. In the example of Figure 9, reconstructing a whole field of view (2472×3296)
 400 and considering the spatial evolution of the PSF takes less 10 minutes. These estimations have
 401 been realized using an Intel Core i9-11950H CPU 2.60GHz with 16GBytes of RAM. This
 402 computational time can be reduced using GPU.

403 5. Conclusion

404 In this article, we present a method to estimate the aberrations and thus reduce reconstruction
 405 errors, by using a more accurate image formation model, in in-line holographic microscopy. This
 406 method is based on the use of calibration beads. We show that the rigorous and highly constrained
 407 Mie model can be used to estimate bead parameters and Zernike coefficients at the same time
 408 with a good precision and repeatability. Moreover, this approach requires only one hologram and
 409 does not require any assumption on the PSF evolution in the field of view. This calibration step
 410 could be done sequentially, like standard calibrations or *in-situ* by inserting calibrated beads in
 411 the biological sample itself. However, this may depend on the application or on the main origin
 412 of the aberrations (from the optical setup or from the sample itself). Actually, adding calibration
 413 beads in the sample has already proven to be useful for autofocusing [23]. In this context, with
 414 the present method of correction of aberrations, this autofocusing would be even more accurate.

415 Once the Zernike coefficients have been estimated, it is then possible to use them in a
 416 regularized approach framework to reconstruct any biological objects (spherical or not), as long
 417 as the sparsity constraint required in in-line digital holography is fulfilled. This methodology of
 418 aberration estimation was applied for the improvement of regularized reconstruction of holograms
 419 with the in-line holographic microscopy configuration. However, it is also applicable to off-axis
 420 holography or other coherent imaging techniques or simply used as a calibration method for
 421 microscopy systems.

422 The method proposed here offers interesting perspectives for reconstructing more accurately
 423 and with more quantitativity the absorption and the phase of the objects of interest, even with
 424 poorly corrected or misaligned optical systems, non-standard optical configurations (various
 425 sample media, variable axial position of the objects below the coverslip) and more generally, for
 426 any non-standard microscopy configurations that may introduce aberrations.

427 In this study, we estimated aberrations parameters on a discrete grid. The next step could be to
 428 interpolate the spatially varying PSF. This PSF can then be used in the image reconstruction step,
 429 but with a high computational cost. Nevertheless, fast algorithms can be used [45, 46].

430 Appendix A : Zernike polynomials

Zernike polynomials depend on two parameters: the azimuthal angle $\phi = \arctan\left(\frac{\kappa_y}{\kappa_x}\right)$ and the
 normalized radial distance $\rho = \frac{\lambda}{\text{NA}} \sqrt{\kappa_x^2 + \kappa_y^2}$ and are defined as follows :

$$Z_n^m(\rho, \phi) = \begin{cases} R_n^{|m|}(\rho) \sin(m\phi) & \text{if } m > 0 \\ R_n^{|m|}(\rho) \cos(m\phi) & \text{otherwise} \end{cases}$$

where $n \in \mathbb{N}$, $m \in \mathbb{Z}$ and $R_n^m(\rho)$ is defined as :

$$R_n^m(\rho) = \sum_{k=0}^{\frac{n-m}{2}} \frac{(-1)^k (n-k)!}{k! \left[\frac{n+m}{2} - k\right]! \left[\frac{n-m}{2} - k\right]!} \rho^{n-2k}$$

431 with $n \geq |m|$ and $n - |m|$ even.

432

433 Because of the numerical aperture, the pupil function is zero out of the disk defined by $\rho \leq 1$.
 434 An illustration of the polynomials is given on Fig. 10 [47].

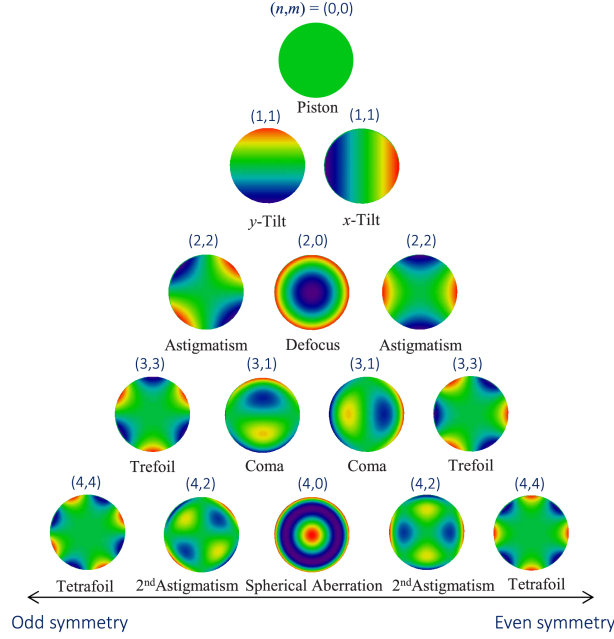


Fig. 10. Illustration of the 15 first Zernike polynomials (adapted from [47]).

435 Appendix B : Theoretical study of the aberration parameters accuracy

436 In this appendix, we aim at estimating the achievable precision on each estimated parameter and to
 437 study the correlation between these parameters. For these purposes, Cramér-Rao Lower Bounds
 438 (CRLB) and the correlation matrix are computed [48] using our aberrated model \mathbf{m}^P presented in
 439 section 2.1 eq. (1). According to Cramér-Rao inequality, the variance of any unbiased estimator
 440 $\hat{\zeta} = \{\zeta_i\}_i = \{\boldsymbol{\theta}, \boldsymbol{\alpha}\}$ of the unknown vector parameter ζ^\dagger is bounded from below by i-th diagonal
 441 coefficient of the inverse of the Fisher information matrix:

$$\text{Var}(\hat{\zeta}_i) \geq [\mathbf{I}^{-1}(\zeta^\dagger)]_{i,i} = \sigma_{\zeta_i}^{\text{CRLB}^2} \quad (8)$$

442 where $\mathbf{I}(\zeta^\dagger)$ is the Fisher information matrix. It is linked to the curvature of the cost function in
 443 the parameters space:

$$[\mathbf{I}(\zeta)]_{i,j} = E \left[\left. \frac{\partial^2 \mathcal{D}^P(\mathbf{d}, \mathbf{m}^P(\cdot))}{\partial \zeta_i \partial \zeta_j} \right|_{\zeta} \right] \quad (9)$$

444 In the case of white Gaussian noise of standard deviation σ_ϵ , neglecting quantization effect
 445 and considering a centered model [49] :

$$[\mathbf{I}(\zeta)]_{i,j} = \frac{1}{\sigma_\epsilon^2} \sum_k \left(\frac{\partial \mathbf{m}^P(x_k, y_k, \zeta)}{\partial \zeta_i} \frac{\partial \mathbf{m}^P(x_k, y_k, \zeta)}{\partial \zeta_j} \right) \quad (10)$$

446 These bounds are computed for a bead at the center of the field of view and for several defocus
 447 distances with parameters of Table 1 ($\boldsymbol{\theta}$ ($x = 0 \mu\text{m}$, $y = 0 \mu\text{m}$, $z, r = 0.5 \mu\text{m}$, $n = 1.58$)).

448 As the aberrations happen to be quite low in our case, the accuracy study has been performed
 449 with Zernike coefficient set to zero. Thus, the accuracy on the Zernike coefficients has been
 450 studied around a zero value.

451 Figure 11 illustrates the evolution of the CRLB with the propagation distance z (*i.e.* the lower
 452 bound variance of each parameter versus z value).

453 These CRLB have been computed considering σ_ϵ constant and using numerical derivatives.
 454 For most parameters the best accuracy is obtained for defocus distances between 10 and 15 μm .
 455 In this study, the defocus distance $z = 12\mu\text{m}$ was considered.

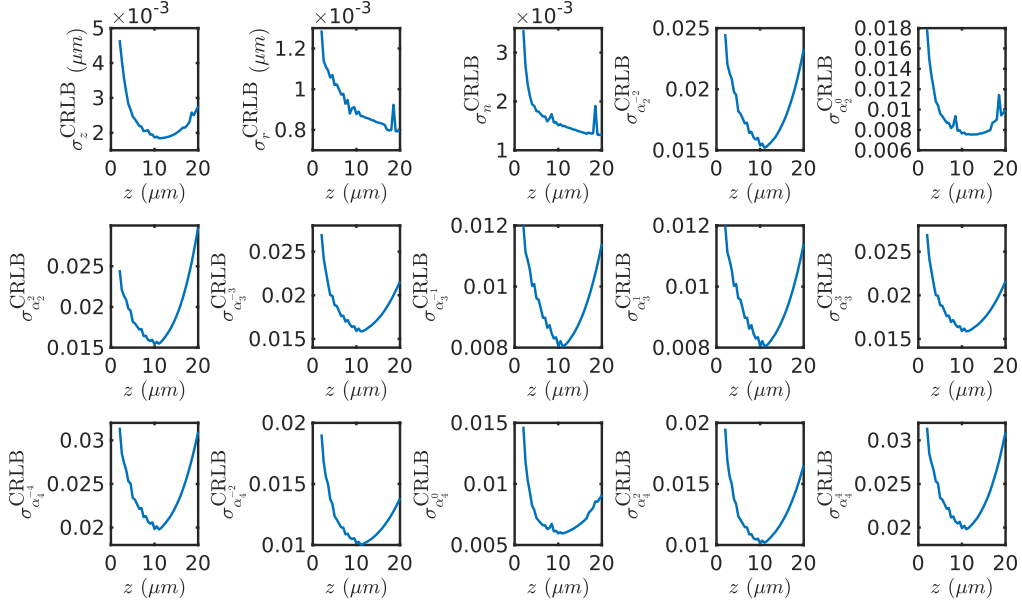


Fig. 11. Evolution of Cramér-Rao Lower Bounds on each parameter as a function of z . The experimental parameters of the model are given in Table 1. These CRLB have been computed for a hologram without aberrations.

456 The correlation matrix Σ is obtained by:

$$\Sigma_{i,j}(\zeta) = \frac{[\mathbf{I}^{-1}(\zeta)]_{i,j}}{\sigma_{\zeta_i}^{\text{CRLB}} \cdot \sigma_{\zeta_j}^{\text{CRLB}}} \quad (11)$$

457 Table 6 shows this correlation matrix for the selected seventeen parameters. Coefficients below
 458 0.05 are set to zero for a better visualization.

459 The correlation matrix indicates strong correlations between several parameters. Unsurprisingly,
 460 r and n are highly correlated as the phase shift induced by an object depends on the product of
 461 these two parameters and the phase shift has a strong effect on the propagation. It is interesting
 462 to notice that coma coefficients represented by α_3^{-1} and α_3^1 are highly correlated with x and
 463 y . Therefore, ignoring the coma aberration could lead to lateral shifts in the reconstructions.
 464 Correlations between α_2^{-4} and α_2^{-2} , α_4^0 and α_2^0 or α_4^2 and α_2^2 , may lead to misestimations of
 465 these coefficients. This is studied in section 4.1 on simulation experiments. However, it would
 466 be probably worse not to take them into account because that would systematically introduce
 467 errors in the model. Most of the other coefficients of the correlation matrix are low or null
 468 and the corresponding parameters can then be considered as decorrelated. Because of the high

	x	y	z	r	n	α_2^{-2}	α_2^0	α_2^2	α_3^{-3}	α_3^{-1}	α_3^1	α_3^3	α_4^{-4}	α_4^{-2}	α_4^0	α_4^2	α_4^4
x	1	0	0	0	0	0	0	0	0	-0.89	0	0	0	0	0	0	0
y	0	1	0	0	0	0	0	0	0	0	-0.89	0	0	0	0	0	0
z	0	0	1	0.24	-0.13	0	-0.49	0	0	0	0	0	0	0	-0.39	0	0
r	0	0	0.24	1	-0.85	0	-0.13	0	0	0	0	0	0	0	0	0	0
n	0	0	-0.13	-0.85	1	0	0.22	0	0	0	0	0	0	0	0.05	0	0
α_2^{-2}	0	0	0	0	0	1	0	0	0	0	0	0	0	0.72	0	0	0
α_2^0	0	0	-0.49	-0.13	0.22	0	1	0	0	0	0	0	0	0	0.92	0	0
α_2^2	0	0	0	0	0	0	0	1	0	0	0	0	0	0	0	0.72	0
α_3^{-3}	0	0	0	0	0	0	0	0	1	0	0	0	0	0	0	0	0
α_3^{-1}	-0.89	0	0	0	0	0	0	0	0	1	0	0	0	0	0	0	0
α_3^1	0	-0.89	0	0	0	0	0	0	0	0	1	0	0	0	0	0	0
α_3^3	0	0	0	0	0	0	0	0	0	0	0	1	0	0	0	0	0
α_4^{-4}	0	0	0	0	0	0	0	0	0	0	0	0	1	0	0	0	0
α_4^{-2}	0	0	0	0	0	0.72	0	0	0	0	0	0	0	1	0	0	0
α_4^0	0	0	-0.39	0	-0.05	0	0.92	0	0	0	0	0	0	0	1	0	0
α_4^2	0	0	0	0	0	0	0	0.72	0	0	0	0	0	0	0	1	0
α_4^4	0	0	0	0	0	0	0	0	0	0	0	0	0	0	0	0	1

Table 6. Correlation matrix of the 5 beads parameters and 12 Zernike coefficients. High correlation or anti-correlations are represented in red, moderate correlation or anti-correlations in yellow, low correlations or anti-correlations in green.

469 correlation values in the correlation matrix, all parameters must be estimated at the same time to
470 prevent estimation errors.

471 **Acknowledgement.** The algorithmic tools presented in this work have been implemented within the
472 framework of the Matlab library GlobalBioIm [50,51] ([https://biomedical-imaging-group.
473 github.io/GlobalBioIm/index.html](https://biomedical-imaging-group.github.io/GlobalBioIm/index.html)). The Zernike polynomials models have been computed
474 using Fricker’s implementation [52] ([https://www.mathworks.com/matlabcentral/
475 fileexchange/7687-zernike-polynomials](https://www.mathworks.com/matlabcentral/fileexchange/7687-zernike-polynomials)). LINCOA optimization strategies have been computed
476 using the PDFO library [53] (<https://www.pdfo.net>, doi:10.5281/zenodo.3887569).

477 **Funding.** This work has been funded by the Auvergne-Rhône-Alpes region, France, under project
478 DIAGHOLO. It was also performed within the framework of the LABEX PRIMES (ANR-11-LABX-0063)
479 of Université de Lyon, within the program "Investissements d’Avenir"(ANR-11-IDEX-0007) operated by
480 the French National Research Agency (ANR).

481 **Disclosures.** The authors declare no conflicts of interest.

482 **Data availability.** Data underlying the results presented in this paper are not publicly available at this time
483 but may be obtained from the authors upon reasonable request.

484 References

- 485 1. R. Alexander, B. Leahy, and V. N. Manoharan, "Precise measurements in digital holographic microscopy by modeling
486 the optical train," *J. Appl. Phys.* **128**, 060902 (2020).
- 487 2. J. G. McNally, T. Karpova, J. Cooper, and J. A. Conchello, "Three-Dimensional Imaging by Deconvolution
488 Microscopy," *Methods* **19**, 373–385 (1999).
- 489 3. P. Sarder and A. Nehorai, "Deconvolution methods for 3-D fluorescence microscopy images," *IEEE Signal Process.
490 Mag.* **23**, 32–45 (2006).
- 491 4. F. Soulez, L. Denis, Y. Tourneur, and E. Thiebaut, "Blind deconvolution of 3D data in wide field fluorescence
492 microscopy," in *2012 9th IEEE International Symposium on Biomedical Imaging (ISBI)*, (IEEE, Barcelona, Spain,
493 2012), pp. 1735–1738.
- 494 5. J. Li, F. Xue, and T. Blu, "Fast and accurate three-dimensional point spread function computation for fluorescence
495 microscopy," *JOSA A* **34**, 1029–1034 (2017). Publisher: Optica Publishing Group.

- 496 6. A. Aristov, B. Lelandais, E. Rensen, and C. Zimmer, "ZOLA-3D allows flexible 3D localization microscopy over an
497 adjustable axial range," *Nat. Commun.* **9**, 2409 (2018).
- 498 7. J. Li, F. Xue, F. Qu, Y.-P. Ho, and T. Blu, "On-the-fly estimation of a microscopy point spread function," *Opt. Express*
499 **26**, 26120–26133 (2018). Publisher: Optica Publishing Group.
- 500 8. S. F. Gibson and F. Lanni, "Experimental test of an analytical model of aberration in an oil-immersion objective lens
501 used in three-dimensional light microscopy," *JOSA A* **8**, 1601–1613 (1991).
- 502 9. V. Lakshminarayanan and A. Fleck, "Zernike polynomials: a guide," *J. Mod. Opt.* **58**, 545–561 (2011).
- 503 10. G. Zheng, X. Ou, R. Horstmeyer, and C. Yang, "Characterization of spatially varying aberrations for wide field-of-view
504 microscopy," *Opt. Express* **21**, 15131 (2013).
- 505 11. P. Ferraro, S. D. Nicola, A. Finizio, G. Coppola, S. Grilli, C. Magro, and G. Pierattini, "Compensation of the inherent
506 wave front curvature in digital holographic coherent microscopy for quantitative phase-contrast imaging," *Appl. Opt.*
507 **42**, 1938–1946 (2003). Publisher: Optica Publishing Group.
- 508 12. T. Colomb, E. Cuche, F. Charrière, J. Kühn, N. Aspert, F. Montfort, P. Marquet, and C. Depeursinge, "Automatic
509 procedure for aberration compensation in digital holographic microscopy and applications to specimen shape
510 compensation," *Appl. optics* **45**, 851–863 (2006).
- 511 13. J. Min, B. Yao, S. Ketelhut, C. Engwer, B. Greve, and B. Kemper, "Simple and fast spectral domain algorithm for
512 quantitative phase imaging of living cells with digital holographic microscopy," *Opt. Lett.* **42**, 227–230 (2017).
- 513 14. L. Xu, X. Peng, J. Miao, and A. K. Asundi, "Studies of digital microscopic holography with applications to
514 microstructure testing," *Appl. Opt.* **40**, 5046–5051 (2001). Publisher: Optica Publishing Group.
- 515 15. J. Garcia-Sucerquia, W. Xu, S. K. Jericho, P. Klages, M. H. Jericho, and H. J. Kreuzer, "Digital in-line holographic
516 microscopy," *Appl. optics* **45**, 836–850 (2006).
- 517 16. T. Kreis, *Handbook of holographic interferometry: optical and digital methods* (John Wiley & Sons, 2006).
- 518 17. G. Popescu, *Quantitative phase imaging of cells and tissues* (McGraw-Hill Education, 2011).
- 519 18. C. Martin, B. Leahy, and V. N. Manoharan, "Improving holographic particle characterization by modeling spherical
520 aberration," *Opt. Express* **29**, 18212 (2021).
- 521 19. T. Olivier, D. Brault, S. Joshi, T. Brard, A. Brodoline, L. Méès, and C. Fournier, "Effects of some model
522 approximations in the reconstructions of digital in-line holograms: simulations, experiments on calibrated objects
523 and model refinement assessment," in *Unconventional Optical Imaging III*, vol. 12136 M. P. Georges, G. Popescu,
524 and N. Verrier, eds., International Society for Optics and Photonics (SPIE, 2022), pp. 7 – 17.
- 525 20. S.-H. Lee, Y. Roichman, G.-R. Yi, S.-H. Kim, S.-M. Yang, A. Van Blaaderen, P. Van Oostrum, and D. G.
526 Grier, "Characterizing and tracking single colloidal particles with video holographic microscopy," *Opt. express* **15**,
527 18275–18282 (2007).
- 528 21. F. Soulez, L. Denis, C. Fournier, É. Thiébaud, and C. Goepfert, "Inverse-problem approach for particle digital
529 holography: accurate location based on local optimization," *JOSA A* **24**, 1164–1171 (2007).
- 530 22. F. C. Cheong, B. J. Krishnatreya, and D. G. Grier, "Strategies for three-dimensional particle tracking with holographic
531 video microscopy," *Opt. express* **18**, 13563–13573 (2010).
- 532 23. D. Brault, C. Fournier, T. Olivier, N. Faure, S. Dixneuf, L. Thibon, L. Mees, and L. Denis, "Automatic numerical
533 focus plane estimation in digital holographic microscopy using calibration beads," *Appl. Opt.* **61**, B345 (2022).
- 534 24. O. Flasseur, C. Fournier, N. Verrier, L. Denis, F. Jolivet, A. Cazier, and T. Lépine, "Self-calibration for lensless color
535 microscopy," *Appl. optics* **56**, F189–F199 (2017).
- 536 25. N. Verrier, C. Fournier, L. Méès, and T. Fournel, "In-line particle holography with an astigmatic beam: setup
537 self-calibration using an "inverse problems" approach," *Appl. optics* **53**, G147–G156 (2014).
- 538 26. L. Denis, D. Lorenz, E. Thiébaud, C. Fournier, and D. Trede, "Inline hologram reconstruction with sparsity constraints,"
539 *Opt. letters* **34**, 3475–3477 (2009).
- 540 27. F. Jolivet, F. Momey, L. Denis, L. Méès, N. Faure, N. Grosjean, F. Pinston, J.-L. Marié, and C. Fournier, "Regularized
541 reconstruction of absorbing and phase objects from a single in-line hologram, application to fluid mechanics and
542 micro-biology," *Opt. express* **26**, 8923–8940 (2018).
- 543 28. J. R. Fienup, "Phase retrieval algorithms: a comparison," *Appl. optics* **21**, 2758–2769 (1982).
- 544 29. T. Lатыchevskaia and H.-W. Fink, "Solution to the twin image problem in holography," *Phys. review letters* **98**, 233901
545 (2007).
- 546 30. A. Tarantola, *Inverse Problem Theory and Methods for Model Parameter Estimation*, vol. 89 (SIAM, 2005).
- 547 31. F. Slimani, G. Gréhan, G. Gouesbet, and D. Allano, "Near-field lorenz-mie theory and its application to microholog-
548 raphy," *Appl. optics* **23**, 4140–4148 (1984).
- 549 32. F. Soulez, L. Denis, É. Thiébaud, C. Fournier, and C. Goepfert, "Inverse problem approach in particle digital
550 holography: out-of-field particle detection made possible," *JOSA A* **24**, 3708–3716 (2007).
- 551 33. L. Méès, N. Grosjean, D. Chareyron, J.-L. Marié, M. Seifi, and C. Fournier, "Evaporating droplet hologram simulation
552 for digital in-line holography setup with divergent beam," *JOSA A* **30**, 2021–2028 (2013).
- 553 34. R. J. Noll, "Zernike polynomials and atmospheric turbulence," *JOSA* **66**, 207–211 (1976).
- 554 35. O. Flasseur, L. Denis, É. Thiébaud, T. Olivier, and C. Fournier, "Expaco: detection of an extended pattern under
555 nonstationary correlated noise by patch covariance modeling," in *2019 27th European Signal Processing Conference*
556 (*EUSIPCO*), (IEEE, 2019), pp. 1–5.
- 557 36. D. Brault, L. Denis, S. Dixneuf, T. Olivier, N. Faure, and C. Fournier, "Fast and robust pattern detection: Application
558 to spherical bead localization in holographic microscopy," (accepted in IEEE European Signal Processing Conference

- 559 (EUSIPCO), 09/2022).
- 560 37. J. W. Goodman, *Introduction to Fourier optics, 3rd ed.* (Roberts & Co. Publishers, Englewood, Colorado, 2004).
- 561 38. S. Sothivirat and J. A. Fessler, "Penalized-likelihood image reconstruction for digital holography," *J. Opt. Soc. Am. A* **21**, 737–750 (2004).
- 562
- 563 39. F. Soulez, M. Rostykus, C. Moser, and M. Unser, "A CONstrained Method for lensless Coherent Imaging of thin samples," *Applied optics* **61**, F34–F46 (2022).
- 564
- 565 40. P. Charbonnier, L. Blanc-Féraud, G. Aubert, and M. Barlaud, "Deterministic edge-preserving regularization in computed imaging," *IEEE Transactions on image processing* **6**, 298–311 (1997).
- 566
- 567 41. A. Beck and M. Teboulle, "Fast gradient-based algorithms for constrained total variation image denoising and deblurring problems," *IEEE transactions on image processing* **18**, 2419–2434 (2009).
- 568
- 569 42. O. Haeberle, "Focusing of light through a stratified medium: a practical approach for computing fluorescence microscope point spread functions. Part II: confocal and multiphoton microscopy," *Optics Communications* **235**, 1–10 (2004).
- 570
- 571
- 572 43. J. Dohet-Eraly, L. Mèès, T. Olivier, F. Dubois, and C. Fournier, "Analysis of three-dimensional objects in quantitative phase contrast microscopy: a validity study of the planar approximation for spherical particles," in *Unconventional Optical Imaging II*, vol. 11351 C. Fournier, M. P. Georges, and G. Popescu, eds., International Society for Optics and Photonics (SPIE, 2020), pp. 76 – 85.
- 573
- 574
- 575
- 576 44. M. J. Powell, "On fast trust region methods for quadratic models with linear constraints," *Math. Program. Comput.* **7**, 237–267 (2015).
- 577
- 578 45. L. Denis, E. Thiébaud, and F. Soulez, "Fast model of space-variant blurring and its application to deconvolution in astronomy," in *2011 18th IEEE International Conference on Image Processing*, (IEEE, 2011), pp. 2817–2820.
- 579
- 580 46. L. Denis, E. Thiébaud, F. Soulez, J.-M. Becker, and R. Mourya, "Fast approximations of shift-variant blur," *Int. J. Comput. Vis.* **115**, 253–278 (2015).
- 581
- 582 47. Y. Hsieh, Y. Yu, Y. Lai, M. Hsieh, and Y.-F. Chen, "Integral-based parallel algorithm for the fast generation of the zernike polynomials," *Opt. Express* **28**, 936–947 (2020).
- 583
- 584 48. S. Kay, "Fundamentals of statistical signal processing: estimation theory," *Technometrics* **37**, 465–466 (1993).
- 585
- 586 49. C. Fournier, L. Denis, and T. Fournel, "On the single point resolution of on-axis digital holography," *JOSA A* **27**, 1856–1862 (2010).
- 587
- 588 50. M. Unser, E. Soubies, F. Soulez, M. McCann, and L. Donati, "Globalbioim: A unifying computational framework for solving inverse problems," in *Computational Optical Sensing and Imaging*, (Optical Society of America, 2017), pp. CTu1B–1.
- 589
- 590 51. E. Soubies, F. Soulez, M. T. McCann, T.-a. Pham, L. Donati, T. Debarre, D. Sage, and M. Unser, "Pocket guide to solve inverse problems with globalbioim," *Inverse Probl.* **35**, 104006 (2019).
- 591
- 592 52. P. Fricker, "Zernike polynomials," *MATLAB Cent. File Exch.* (2022).
- 593 53. T. M. Ragonneau and Z. Zhang, "PDFO: cross-platform interfaces for powell's derivative-free optimization solvers (version 1.1)," (2021).
- 594